Energy-Based Analysis and Predictive Variable Frequency Control Scheme of a High-Voltage Solid State Pulse Generator for Space Applications

Chinara Kuldip, *Graduate Student Member, IEEE*, and Lakshmi Narasamma N, *Senior Member, IEEE*

***Abstract*—Pulsed plasma thrusters (PPT) hold significant promise for space exploration and exploitation by integrating high-power capabilities of magneto-plasmadynamic (MPD) thrusters with low average power consumption (typically <150 W) and reduced heat generation. These thrusters are powered by high-voltage pulse generator with peak pulse magnitude ranging from 250 V to 2.5 kV. Pulse generators in the literature often exhibit longer charging times, which limit the pulse repetitive rate (PRR) to below 500 pulses per second and prevent it from achieving the desired pulse voltage profile. This article proposes a resonant-based high-voltage pulse generator that features programmability for pulse amplitude, enhanced PRR, reduced full width at half maximum (FWHM), and improved efficiency, addressing the requirements of the PPT. A predictive control scheme is proposed for the variable frequency-based high-voltage pulse generator, eliminating the need for current and voltage sensors; reducing system costs, associated conduction losses, and control complexity compared to conventional control methods. An energy-based analysis is used to investigate the impact of parasitics in the pulse generator deriving essential parameters for PPT operation and offering an improved analytical approach. The energy-based analysis, derived analytical expressions and proposed control scheme are validated through experimental testing for pulse voltage of −2.5 kV, with a PRR of 1000 Hz and a FWHM of 20 μs. The proposed control scheme achieves precise tracking of the MOSFET turn-ON and turn-OFF instants, reducing timing errors to less than 5% compared to conventional control methods.**

***Index Terms*—Energy-based analysis, parasitic capacitance, predictive control, programmable pulse voltage, pulse plasma thrusters (PPTs), pulse power supply, space application.**

I. Introduction

THE utilization of small satellites has rapidly expanded for applications in earth observation, remote sensing, telecommunications, and scientific research [1], creating a need for compact and cost-effective systems. Pulsed plasma thrusters (PPTs) are emerging as replacements for conventional magneto-plasmadynamic (MPD) thrusters [2], offering characteristics ideally suited to provide a straightforward, lightweight, compact, and high-performance propulsion solution for power-limited small satellites [3]. The PPTs feature a low average power consumption (typically below 150 W) and minimized heat generation, making them well-suited for these applications.

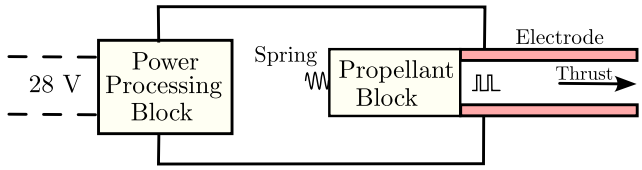

Fig. 1. Block diagram of a typical pulse plasma thruster (PPT).

Fig. 1 presents the block diagram of the PPT. When a high voltage (HV) is applied across two electrodes, it initiates an arc that heats and decomposes the Teflon propellant into ionized plasma, which is then accelerated by the Lorentz force to produce thrust [4]. The electrical power supply to the PPT (i.e., the "Power Processing Block" in Fig. 1) is the critical component and should prioritize cost-effectiveness and compactness, while also featuring high power density and efficiency with low average power consumption. Utilizing a nonpulsed HV power supply increases the average power rating and size of the supply [5], which is impractical for small satellites where mass and power are constrained. On the other hand, pulse power supplies fulfill the requirements of the power processing block, making them suitable for use [6].

Converter topologies used in the literature for pulse power supplies of PPT often incorporate HV switches alongside precharging configurations to generate the necessary pulse profile [6], [7], [8]. However, these precharging setups typically feature longer charging time constants, resulting in either a reduced pulse repetitive rate (PRR) or an inability to reach the desired peak pulse amplitude [9]. Furthermore, the achievable efficiency and the full width at half maximum (FWHM) of the pulse power supply are affected by factors such as high turn-ON resistance (in 100 Ωs), built-in snubbers, and the minimum pulse width limitation of the high-voltage switch [10]. Increased overshoots and undershoots during pulsing contribute to the erosion of the cathode and anode electrodes of the PPT. In addition, these high-voltage switches tend to be bulky and are primarily suitable for high-pulse power applications (in the range of 1 to 5 kW). When a resonant-based high-voltage, high-power pulse generator is used for low-power applications, the FWHM and

Received 12 September 2024; revised 3 December 2024; accepted 8 January 2025. Date of publication 14 January 2025; date of current version 26 February 2025. Recommended for publication by Associate Editor M. Ponce-Silva. *(Corresponding author: Chinara Kuldip.)*

The authors are with the Department of Electrical Engineering, Indian Institute of Technology Madras, Chennai 600036, India (e-mail: kuldip.chinara@gmail.com).

Color versions of one or more figures in this article are available at https://doi.org/10.1109/TPEL.2025.3528832.

Digital Object Identifier 10.1109/TPEL.2025.3528832

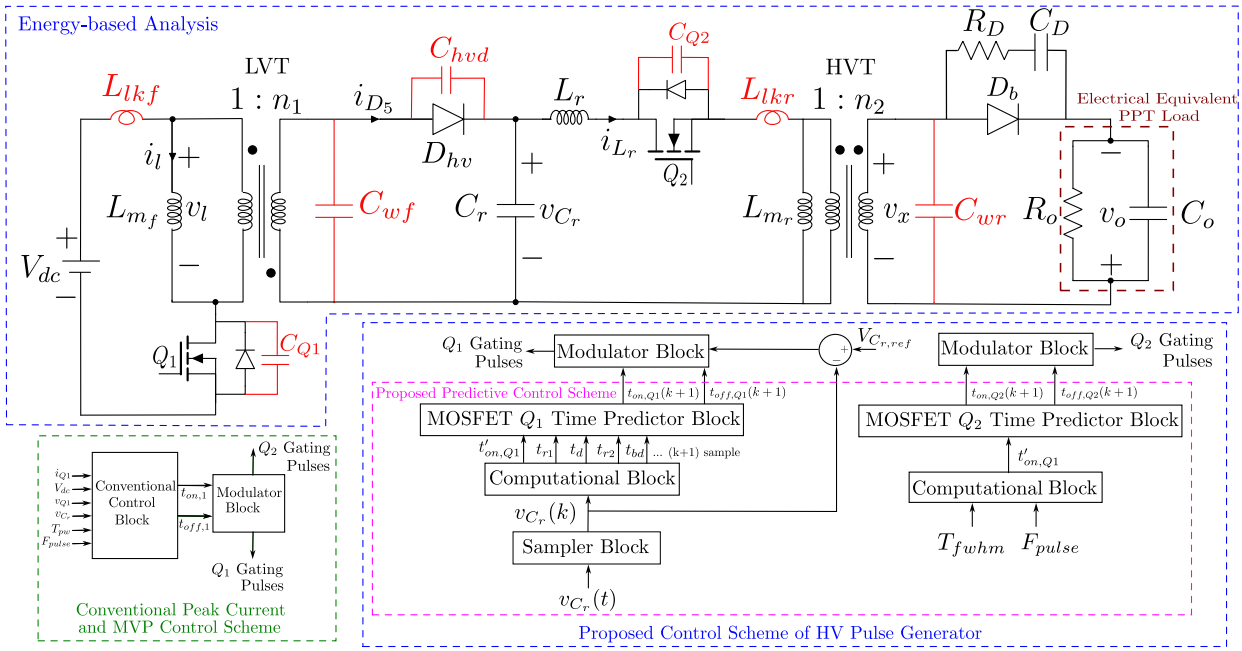

Fig. 2. Resonant flyback topology with proposed predictive variable frequency control scheme.

PRR are often reduced to meet the load's energy requirements. High-power systems tolerate higher losses due to their larger absolute power transfer. However, in low-power applications like space plasma thrusters, even small losses significantly impact efficiency, making stringent efficiency requirements essential.

Most existing literature addresses high-current resonant-based pulsed applications with highly inductive loads or continuous sinusoidal voltage or current pulses. However, there is limited focus on converters achieving soft switching during pulsing. In [11], [12], resonant pulse power supplies are designed for high-current sinusoidal pulse applications but do not incorporate soft-switching techniques. In [13], a bidirectional short high-voltage pulse topology is presented, yet it lacks the capability for soft switching. In [14], a soft-switched topology for short high-current pulses is introduced, but the power requirements for these converters typically range from several kilowatts. In contrast, the proposed application in this work targets a low-power scenario ($<$ 150 W) and demands a short high voltage unidirectional pulse. Fig. 2 illustrates the proposed HV pulse generator for PPT. The proposed resonant flyback topology features a compact structure with a reduced component count, galvanic isolation, higher PRR ($>$ 1000 Hz), and less FWHM ($<$ 30μs), meeting the requirements of the PPT. In addition, it demonstrates efficiency ($\eta > 90\%$) for low-power applications [15]. This topology avoids the need for snubbers by integrating ZVS turn-ON and ZCS turn-OFF in the control scheme for switches Q_1 and Q_2, respectively.

Due to the larger secondary turns and winding arrangements in the low voltage transformer (LVT) and high voltage transformer (HVT) of the resonant flyback converter, the leakage inductance and the winding capacitance of the transformers increase [16]. These parasitics, which include the semiconductor devices' node capacitances and transformer leakage inductance and winding capacitance (illustrated in red in Fig. 2), significantly impact the performance of the capacitive-dominant PPT load [17], [18], [19]. Neglecting these parasitics can result in failing to achieve the desired pulse voltage profile, and therefore, analyzing the converter considering all the parasitics is essential [20]. Circuit-based analysis of the resonant flyback converter is accurate, but it does not provide insights into the energy exchanges occurring in the converter. Furthermore, determining the operating point and control parameters of the converter using this method is complex. The energy-based analysis is straightforward, facilitating the derivation of simple expressions for control implementation and the judicious selection of resonant flyback topology. It also aids in determining essential parameters. In [9], an energy-based analysis is proposed to evaluate the feasibility of using a flyback converter-based high-voltage pulse generator for applications with power requirements below 150 W. Similarly, Ravi et al. [21] employed an energy-based approach for charging a flyback converter from 12 to 2500 V, specifically targeting battery-powered capacitive load applications. Building on these approaches, this article employs an energy-based analysis that governs the energy exchanges in the pulse generator with dominant parasitic effects.

In Fig. 2, the green box illustrates the conventional control scheme featuring peak current mode (PCM) and minimum voltage point (MVP) control, which involve sensing the switch Q_1 current and voltage as well as sensing the input voltage (V_{dc}) and the resonant capacitor voltage (v_{C_r}) to generate the gating pulses [9]. The inclusion of current transformers (CTs) for precise MOSFET current sensing results in notable conduction losses in the sensor [22]. The use of current or voltage sensors increases the overall cost of the converter, and these sensors often have relatively slow response times. In addition, achieving high accuracy with sensors that measure pulse loads in the kilovolt range is challenging and undesirable [23]. The voltage drop caused by parasitic elements and MOSFET turn-ON

resistance adds to the voltage sensor, posing challenges in precise sensing of the MOSFET voltage. In addition to the sensors, supplementary analog circuitry is incorporated for generating gating pulses for Q_1 and Q_2 which increases both the cost and complexity of the converter system [9]. In [24], a model predictive control strategy is discussed for dual-active-bridge converters in pulse power applications, which introduces a cost function for resonance damping of load voltage. Zhang et al. [25] presented model predictive control for a three-level bidirectional dc–dc converter to stabilize the dc bus voltage for stable charge/discharge of super capacitor. However, these topologies use fixed switching frequencies, limiting efficiency and performance in high voltage pulse power applications requiring soft-switching and variable-frequency operation to reduce losses and handle dynamic loads [26]. Despite this, research on soft-switched, variable-frequency predictive control for high-voltage pulse power converters remains limited. Therefore, this article proposes a predictive peak current and MVP control scheme for a resonant flyback topology to manage energy flow from the input to the pulsed output, as illustrated in the blue box in Fig. 2.

Predictive control is becoming increasingly favored in converter control systems due to its ability to swiftly converge to the set point of desired parameters accurately, relying on mathematical models. The predictive control techniques involve computing and predicting the future behavior of the converter to achieve predefined control objectives [27], [28], [29]. This article focuses on achieving faster charging of the resonant capacitor (C_r) through predictive control, contrasting it with the conventional sensor-based control method. During the converter operation, attaining precise turn-ON and turn-OFF instances are essential for achieving a faster charging of the resonant capacitor. During the converter operation, the resonant capacitor voltage is sensed during each turn-ON instant of Q_1, facilitating the prediction of turn-ON and turn-OFF instant of Q_1. Similarly, the FWHM and the PRR obtained from the pulse voltage profile are used to calculate the turn-ON and turn-OFF instant of Q_2.

The analysis summarized above underscores the need for an energy-based analysis and control scheme for the pulse generator for PPT. The contributions of this work, detailed through the proposed pulse generator, are summarized below, with key research contributions highlighted in the blue box of Fig. 2.

1) An energy-based analysis is employed to investigate the impact of the parasitics of the resonant flyback topology and derive the essential parameters required for PPT operation.
2) A predictive peak current and MVP control scheme for the resonant flyback topology, controlling the energy flow from input to the pulsed output and eliminating the need for current and voltage sensors, is proposed in this article.
3) Precise extraction of parasitics of the LVT and HVT is obtained experimentally.
4) The proposed model offers programmability in the pulsed voltage profile, enabling the attainment of varying levels of thrust required by the PPT.
5) The proposed energy-based model and predictive control algorithm outlined above is implemented and verified experimentally for a pulsed output voltage of −2.5 kV with the PRR restricted to 1 kHz and the FWHM limited to 20 μs.

II. Circuit-Based Analysis of Resonant Flyback Topology

The proposed resonant flyback converter featuring a variable frequency control scheme is shown in Fig. 2. This converter consists of a high-frequency capacitor precharging network and a resonant pulse frequency network followed by a high-voltage pulse transformer. The converter's steady-state operation is segmented into eight intervals (shown in Fig. 3), with analytical waveforms illustrated in Fig. 4.

Assumptions:

1) The parasitics (semiconductor devices' node capacitances, transformer leakage inductance, and winding capacitance) dominate the conduction losses of the converter.
2) The resonant capacitor (C_r) is assumed to be large enough to maintain a constant voltage throughout a switching cycle.
3) The resonant magnetizing inductance of HVT $L_{m_r} \gg L_r + L_{lkr}$; thus is neglected in the analysis.
4) In order to precharge the resonant capacitor before the gating pulse of Q_2, the switching frequency of Q_1 is maintained significantly higher than that of Q_2.

A. Load Parameters of PPT

A typical PPT load consists of an active electrode, a ground electrode, a dielectric layer (Teflon in this case), and a discharge gap (as shown in Fig. 1). In this article, electrodes with dimensions of 40 cm × 22 cm are chosen. The load includes a 1-mm-thick Teflon dielectric layer, with a 2 mm gap separating the two electrodes. Based on these specifications, the PPT load is electrically represented as a capacitance in parallel with a resistance, where the capacitance (C_o) and resistance (R_o) are estimated to be approximately 300 pF and 100 kΩ, respectively, calculated using the formula in [31].

B. Principle of Operation

The converter operates with a hybrid control scheme to cater to the pulse voltage profile at the output. A predictive variable frequency control scheme generates gating pulses for Q_1, facilitating soft-switching and precharging of the resonant capacitor to the desired value before the gating pulse to Q_2. Subsequently, the gating pulse to Q_2 is determined by a computational block based on the PRR and FWHM of the pulse.

1) *Interval 1 (t_0 to t_1):*
   Initial condition(s): $v_{C_r}(t_0) = V_{C_{r,\max}}$
   At t_0, Q_2 is turned ON, D_b is forward biased, and an L-C resonant loop is formed with the resonant frequency defined by (1), as shown in Fig. 3(a)

$$w_{r_1} = \sqrt{\frac{n_2^2(C_{wr} + C_o) + C_r}{(L_r + L_{lkr})\, n_2^2(C_{wr} + C_o)C_r}}. \tag{1}$$

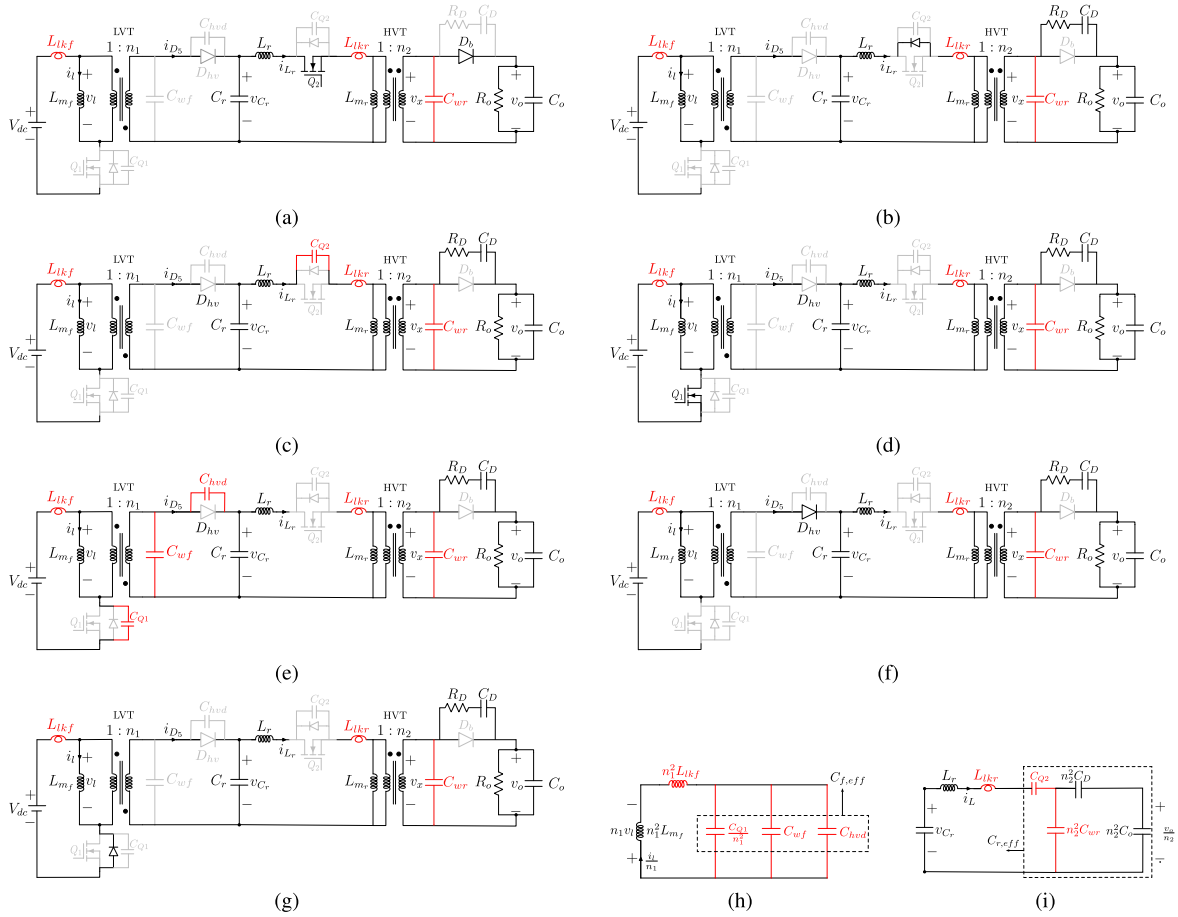

Fig. 3. Equivalent circuit of resonant flyback converter at different time intervals (a) interval 1, (b) interval 2, (c) interval 3, (d) interval 4, (e) interval 5 and 7, (f) interval 6, (g) interval 8, (h) simplified equivalent circuit during interval 5 and 7, (f) simplified equivalent circuit during interval 3.

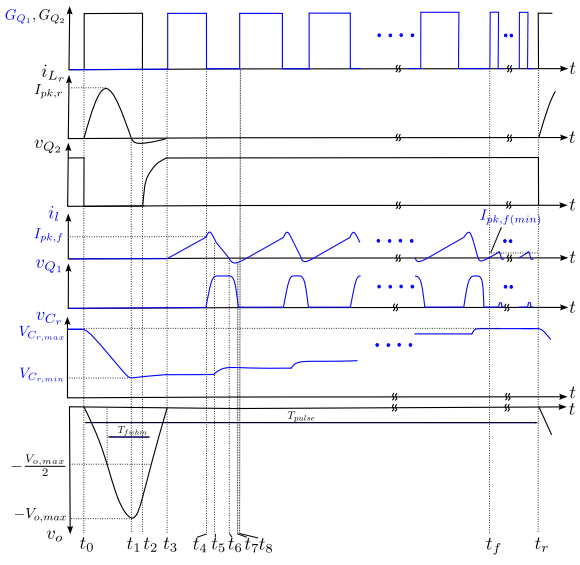

Fig. 4. Steady-state analytical waveforms of the resonant flyback topology.

During this interval, the resonant capacitor discharges to the load and the load voltage (v_o) rises to $V_{o,\max}$, as shown in Fig. 4.

2) *Interval 2 (t_1 to t_2):*
Initial condition(s): $v_{C_r}(t_1) = V_{C_{r,\min}}$, $v_o(t_1) = V_{o,\max}$
At t_1, the body diode of Q_2 is forward-biased and D_b is reverse-biased due to reversal in i_{L_r}. The output voltage discharges through the body diode of Q_2 to charge the resonant capacitor, as illustrated in Fig. 3(b). During this interval, Q_2 is turned OFF, facilitating ZCS turn-OFF of Q_2 as shown in Fig. 4.

3) *Interval 3 (t_2 to t_3):*
Initial condition(s): $v_{Q_2}(t_2) = 0$
At t_2, the body diode of Q_2 becomes reversed-biased (as depicted in Fig. 3(c), causing the current i_{L_r} to charge the equivalent resonant parasitic capacitance ($C_{r,\text{eff}}$) and the resonant capacitor. The simplified circuit is shown in Fig. 3(i). At t_3, C_{Q2} is charged completely, leading to the buildup of reverse voltage across Q_2, as shown in Fig. 4. The output voltage falls to zero with a time constant defined by R_D, C_D, R_o, and C_o.

4) *Interval 4 (t_3 to t_4):*
Initial condition(s): $v_{Q_2}(t_3) = V_{Q2,\max}$, $v_{C_r}(t_3) = (V_{C_{r,\min}} + \Delta V_{C_{r0}})$, $\Delta V_{C_{r0}} = (v_{C_r}(t_3) - v_{C_r}(t_1))$
At t_3, Q_1 is turned ON as shown in Fig. 3(d). During this interval, the current through the magnetizing inductance of LVT (i_l) rises with a slope V_{dc}/L_{m_f} as shown in Fig. 4.

5) *Interval 5 (t_4 to t_5):*
Initial condition(s): $i_l(t_4) = I_{pk,f}$
At t_4, i_l reaches $I_{pk,f}$ and Q_1 is turned OFF via PCM control. During this interval, a portion of the energy stored in the magnetizing inductance (L_{m_f}) is utilized to charge the equivalent flyback parasitic capacitance ($C_{f,\text{eff}}$), as depicted in Fig. 3(e) and 3(h). As a result, the current through i_l decreases, and the voltage across Q_1 rises to $V_{\text{dc}} + v_{C_r}/n_2$ as shown in Fig. 4.
6) *Interval 6 (t_5 to t_6):*
Initial condition(s): $v_{Q1}(t_5) = V_{\text{dc}} + v_{C_r}/n_2$
At t_5, D_{hv} becomes forward-biased and v_{Q1} is clamped to $V_{\text{dc}} + v_{C_r}/n_2$ [shown in Fig. 3(f)]. During this interval, the remaining energy in L_{m_f} is utilized to charge the resonant capacitor as depicted in Fig. 4.
7) *Interval 7 (t_6 to t_7):*
Initial condition(s): $i_l(t_6) = 0$
At t_6, D_{hv} is reverse-biased and during this interval the energy stored in $C_{f,\text{eff}}$ discharges to L_{m_f}, shown in Fig. 3(e) and Fig. 4. At t_7, i_l is negative and when $v_{C_r} > n_1 V_{\text{dc}}$, the body diode of Q_1 is forward biased.
8) *Interval 8 (t_7 to t_8):*
Initial condition(s): $v_{Q_1}(t_7) = 0$
The energy stored in L_{m_f} (during Interval 7) transfers back to the source [shown in Fig. 3(g)] due to the conduction of the body diode of Q_1. During this interval, the gating pulse is given to Q_1, ensuring ZVS turn ON. This switch turn-ON technique is known as MVP control scheme [9], [30].

The time interval from t_3 to t_8 is subsequently repeated until the resonant capacitor charges to $V_{C_{r,\text{max}}}$ at t_f (shown in Fig. 4). The time required to charge the resonant capacitor from $V_{C_{r,\text{min}}}$ to $V_{C_{r,\text{max}}}$ is given by $T_{\text{chrg}} = N_f(t_8 - t_3)$, where N_f represents the number of switching cycles of Q_1 needed to accomplish this precharging process. To sustain the voltage across the resonant capacitor at $V_{C_{r,\text{max}}}$, a minimum peak current ($I_{pk,f(\text{min})}$) is maintained to provide the necessary circulating energy for the parasitics in the converter. The energy stored in $C_{r,\text{eff}}$ during the interval 3 gets discharged before the turn-ON of Q_2 at t_r. From Fig. 4, some of the essential timing parameters of the resonant flyback converter are derived and shown below.

i) The PRR of the converter is defined as $F_{\text{pulse}} = \frac{1}{T_{\text{pulse}}}$; where $T_{\text{pulse}} = t_r - t_0$.
ii) The FWHM of the pulse is defined as time interval between the rising and falling instant of the pulse, where the voltage reaches 50% of $V_{o,\text{max}}$, denoted as T_{fwhm}.
iii) The time required to charge the resonant capacitor from $V_{C_{r,\text{min}}}$ to $V_{C_{r,\text{max}}}$ is given by $T_{\text{chrg}} = N_f(t_8 - t_3)$.
iv) The maximum charging time to charge the resonant capacitor is defined as $T_{\text{chrg(max)}} < T_{\text{pulse}} - T_{\text{fwhm}}$.
v) The rise time of the pulse is defined as $T_{\text{rise}} = t_1 - t_0$.

C. Limitation of Circuit-Based Analysis

1) The circuit-based analysis yields complex and transcendental equations. Thus, computationally intensive processes are needed to derive the control algorithm of the pulse power converter [9].
2) The circuit-based analysis falls short in capturing the energy exchanges within the pulse power converter, thereby obscuring the impact of parasitic elements.
3) The circuit-based analysis falls short in determining the essential parameters of the converter, such as the optimum T_{chrg} such that the resonant capacitor gets charged to $V_{C_{r,\text{max}}}$ before the turn-ON of Q_2, N_f, the variation in resonant capacitor voltage with each switching cycle of Q_1, the threshold energy required to sustain voltage across the resonant capacitor, the average power demand of the load and the pulse load efficiency.

Therefore, this article employs an energy-based analysis to overcome the aforementioned limitations.

III. Proposed Energy-Based Model

In an ideal resonant flyback converter, an energy storage and release interval exists to transfer energy from the source to the load. During the energy storage interval, the resonant capacitor is charged from $V_{C_{r,\text{min}}}$ to $V_{C_{r,\text{max}}}$ over N_f switching cycles of Q_1, as described by

$$\Delta E_{C_r} = \frac{1}{2} C_r \left(V_{C_{r,\text{max}}}^2 - V_{C_{r,\text{min}}}^2 \right) = N_f \frac{1}{2} L_{m_f} I_{pk,f}^2. \quad (2)$$

During the energy release interval, the energy stored in the resonant capacitor is discharged to the load capacitor, as specified by

$$\Delta E_{C_r} = \frac{1}{2} C_o V_{o,\text{max}}^2. \quad (3)$$

In practical scenarios, a notable amount of energy is lost during the energy transfer process due to the presence of parasitic elements. Consequently, additional energy transfer intervals occur alongside the energy storage and energy release intervals.

1) *Interval 1:* Before Q_2 turns ON, the energy stored in $C_{r,\text{eff}}$ ($E_{C_{r,\text{eff}}}$) discharges from v_{C_r} to zero and is transferred to the resonant capacitor. When Q_2 turns ON, the energy stored in the resonant capacitor (E_{C_r}) charges the output capacitor C_o to its maximum voltage $V_{o,\text{max}}$. Hence, the energy delivered to the load is given by

$$E_{C_o} = \frac{1}{2} C_o V_{o,\text{max}}^2 = E_{C_r} + E_{C_{r,\text{eff}}} - \frac{1}{2} L_r I_{pk,r}^2. \quad (4)$$

2) *Interval 2:* As Q_2 turns OFF, $C_{r,\text{eff}}$ charges from zero to v_{C_r}

$$E_{C_{r,\text{eff}}} = \frac{1}{2} C_{r,\text{eff}} v_{C_r}^2 \quad (5)$$

The resonant capacitor must reach $V_{C_{r,\text{max}}}$ before the next turn-ON of Q_1 occurs, which happens at t_r (as illustrated in Fig. 4). This necessitates N_f switching cycles of Q_1 to charge the resonant capacitor. Therefore, the energy exchanges of a single switching cycle of Q_1 are explained from intervals 3 to 7.
3) *Interval 3:* During the turn-ON of Q_1, the energy stored by the magnetizing inductance of LVT is modulated by PCM

control is given as follows:

$$E_{L_{m_f}} = \frac{1}{2} L_{m_f} I_{pk,f}^2. \tag{6}$$

4) *Interval 4:* Some fraction of energy stored in $E_{L_{m_f}}$ is utilized to charge $C_{f,\text{eff}}$ from $-n_1 V_{\text{dc}}$ to v_{C_r} and is given as follows:

$$E_{C_{f,\text{eff}}} = \frac{1}{2} C_{f,\text{eff}} \left(v_{C_r}^2 - n_1^2 V_{\text{dc}}^2 \right). \tag{7}$$

5) *Interval 5:* The remaining energy stored in $E_{L_{m_f}}$ is transferred to the resonant capacitor through the conduction of D_{hv}. Therefore, the energy delivered to C_r in one switching cycle of Q_1 is expressed by

$$\begin{aligned} E_{C_r,\text{cycle}} &= E_{L_{m_f}} - E_{C_{f,\text{eff}}} \\ &= \frac{1}{2} L_{m_f} I_{pk,f}^2 - \frac{1}{2} C_{f,\text{eff}} \left(v_{C_r}^2 - n_1^2 V_{\text{dc}}^2 \right). \end{aligned} \tag{8}$$

6) *Interval 6:* During this interval, the energy stored by $C_{f,\text{eff}}$ during interval 4 is circulated back to L_{m_f}, and this energy circulation ceases when the body diode of Q_1 conducts, i.e., when $v_{C_r} > n_1 V_{\text{dc}}$.
7) *Interval 7:* Upon the turn-ON of the body diode of Q_1, all the energy stored in L_{m_f} is transferred back to the source. During this interval, the gating pulse for Q_1 is given, ensuring ZVS turn-ONof Q_1 via MVP control scheme.

The interval from 3 to 7 is iterated until v_{C_r} reaches $V_{C_{r,\max}}$ at t_f (as depicted in Fig. 4). Let $v_{C_r}(t_3) = v_p$, and v_{p+1} is the voltage attained by the resonant capacitor at the end of the first switching cycle. The energy balance equation from interval 3 to 7 is expressed by

$$E_{C_r(p+1)} = E_{C_r(p)} + E_{L_{mf}} - E_{C_{f,\text{eff}}(p+1)} \tag{9}$$

where $E_{C_r(p)}$ and $E_{C_r(p+1)}$ represent the initial energy at t_3 and the energy attained by the resonant capacitor at the end of the first switching cycle of Q_1, respectively. $E_{C_{f,\text{eff}}(p+1)}$ denotes the energy utilized by $C_{f,\text{eff}}$ in the first switching cycle of Q_1

$$E_{C_r(p+1)} = \frac{1}{2} C_r v_{p+1}^2 \tag{10}$$

$$E_{C_r(p)} = \frac{1}{2} C_r v_p^2 \tag{11}$$

$$E_{C_{f,\text{eff}}(p+1)} = \frac{1}{2} C_{f,\text{eff}} \left(v_{p+1}^2 - n_1^2 V_{\text{dc}}^2 \right). \tag{12}$$

Putting (10)–(12) in (9),

$$\begin{aligned} E_{C_r(p)} + E_{in} &= \frac{1}{2} C_{f,\text{eff}} v_{p+1}^2 + \frac{1}{2} C_r v_{p+1}^2 \\ &= \frac{1}{2} C_r v_{p+1}^2 \left(1 + \frac{C_{f,\text{eff}}}{C_r} \right) \end{aligned} \tag{13}$$

where

$$E_{in} = \frac{1}{2} \left(L_{mf} I_{pk,f}^2 + n_1^2 V_{\text{dc}}^2 C_{f,\text{eff}} \right). \tag{14}$$

Putting $q = (1 + \frac{C_{f,\text{eff}}}{C_r})$ in (13),

$$E_{C_r(p)} + E_{in} - q E_{C_r(p+1)} = 0. \tag{15}$$

The energy balance equation of the first switching cycle of Q_1 is represented by (15). Essential parameters for the design and control of the resonant flyback converter are derived using the energy equations obtained from (4) to (15), and they are presented below.

A. Predicting the Value of v_{C_r} at t_3

The value of v_{C_r} at t_3 is crucial in estimating the number of switching cycles of Q_1 needed to charge the resonant capacitor before the turn-ON of Q_2. From (4) and (5), the energy discharged from $C_{r,\text{eff}}$ is equal to the energy charged into $C_{r,\text{eff}}$ during the switching transition of Q_2

$$\frac{1}{2} C_r \left(v_p^2 - V_{C_{r,\min}}^2 \right) = \frac{1}{2} C_{r,\text{eff}} V_{C_{r,\max}}^2 \tag{16}$$

$$v_p = \sqrt{\frac{C_{r,\text{eff}}}{C_r} V_{C_{r,\max}}^2 + V_{C_{r,\min}}^2} = v_{C_r}(t_3). \tag{17}$$

B. Predicting the Minimum Peak Current Flowing Through the Magnetizing Inductance of LVT to Charge the Resonant Capacitor From $V_{C_{r,min}}$ to $V_{C_{r,max}}$

During each switching cycle of Q_1, the voltage v_{C_r} rises, leading to an increase in $E_{C_{f,\text{eff}}}$ and a decrease in the energy delivered to the load [as referred to in (7) and (8)]. Eventually, at a certain point in time, when $E_{C_{f,\text{eff}}} = E_{L_{m_f}}$, the energy delivered to the load becomes zero, causing v_{C_r} to stop increasing. Therefore, the minimum peak current flowing through the magnetizing inductance of LVT can be determined from (20)

$$E_{L_{m_f}} = E_{C_{f,\text{eff}}}\big|_{v_{C_r} = V_{C_{r,\max}}} \tag{18}$$

$$\frac{1}{2} L_{m_f} I_{pk,f(\min)}^2 = \frac{1}{2} C_{f,\text{eff}} \left(V_{C_{r,\max}}^2 - n_1^2 V_{\text{dc}}^2 \right) \tag{19}$$

$$I_{pk,f(\min)} = \sqrt{\frac{C_{f,\text{eff}} \left(V_{C_{r,\max}}^2 - n_1^2 V_{\text{dc}}^2 \right)}{L_{m_f}}}. \tag{20}$$

If operated with the minimum peak current obtained in (20), the voltage across the resonant capacitor charges to $V_{C_{r,\max}}$. However, this process will take longer than the maximum charging time defined in Section II-B), leading to uneven peak pulse amplitudes, which is undesirable. To ensure that the charging time remains within acceptable limits and that the power does not exceed 150 W (refer Section I), an optimal peak current through the magnetizing inductance of LVT must be designed.

C. Estimating the Optimal Peak Current Flowing Through the Magnetizing Inductance of LVT to Charge the Resonant Capacitor From $V_{C_{r,min}}$ to $V_{C_{r,max}}$ Within $T_{chrg(max)}$

From (8), the energy stored by the magnetizing inductance of LVT is given by the following:

$$E_{L_{m_f}} = E_{C_r,\text{cycle}} + \frac{1}{2} C_{f,\text{eff}} \left(v_{C_r}^2 - n_1^2 V_{\text{dc}}^2 \right). \tag{21}$$

The energy stored by the resonant capacitor to charge from $V_{C_{r,\min}}$ to $V_{C_{r,\max}}$ within $T_{\text{chrg(max)}}$ per switching cycle of Q_1 is

given by

$$E_{C_{r,\text{cycle}}} = \frac{C_r\left(V_{C_{r,\max}}^2 - V_{C_{r,\min}}^2\right)}{2T_{\text{chrg}(\max)}f_{Q_1}} \tag{22}$$

where f_{Q_1} is the switching frequency of Q_1. Using (22) in (21), putting $v_{C_r} = V_{C_{r,\max}}$ and solving for $I_{pk,f}$,

$$I_{pk,f} = \sqrt{\frac{1}{\eta_f L_{m_f}}\left[2E_{C_{r,\text{cycle}}} + C_{f,\text{eff}}\left(V_{C_{r,\max}}^2 - n_1^2 V_{\text{dc}}^2\right)\right]} \tag{23}$$

where η_f is the efficiency of the precharging stage of the resonant capacitor and $I_{pf,f}$ is the optimal peak current flowing through the magnetizing inductance of LVT.

D. Estimating the Number of Cycles Required to Charge the Resonant Capacitor Within $T_{chrg(max)}$

Equation (15) is rewritten by putting $p = p+1, p+2, \ldots p+N_f$ and solving all N_f equations to derive the equation for N_f^{th} switching cycles of Q_1 shown in

$$E_{C_r(p+N_f)} = \frac{E_{C_r(p)} + E_{in}\left(1 + q + q^2 + \cdots + q^{N_f-1}\right)}{q^{N_f}}. \tag{24}$$

Thus,

$$N_f = \frac{\log\left(\frac{\frac{E_{in}}{q-1} - E_{C_{r(p)}}}{\frac{E_{in}}{q-1} - E_{C_{r(p+N)}}}\right)}{\log(q)} \tag{25}$$

where

$$E_{C_r(p+N)} = \frac{1}{2}C_r V_{C_{r,\max}}^2. \tag{26}$$

E. Predicting the Increment in the Resonant Capacitor Voltage Per Switching Cycle of Q_1

Let, in a switching cycle of Q_1, the resonant capacitor voltage increases by Δv_{C_r}. Putting $v_{p+1} = v_p + \Delta v_{C_r}$ in (13)

$$\frac{1}{2}C_r v_p^2 + E_{in} = \frac{1}{2}qC_r(v_p + \Delta v_{C_r})^2 \tag{27}$$

$$\Rightarrow \Delta v_{C_r} = \frac{E_{in} - \frac{1}{2}C_{f,\text{eff}}v_p^2}{qC_r v_p}. \tag{28}$$

F. Predicting the Average Output Power and Pulse Load Efficiency of the Converter

The average output pulse power and the efficiency of the converter are obtained as follows:

$$P_{C_o} = P_{\text{pulse},pk}T_{\text{fwhm}}F_{\text{pulse}} \tag{29}$$

$$\eta = \frac{P_{\text{pulse},pk}T_{\text{fwhm}}F_{\text{pulse}}}{0.5(L_{m_f} + L_{lkf})I_{pk,f}^2 f_{Q1}} \tag{30}$$

where $P_{\text{pulse},pk}$ is the peak pulse power.

G. Predicting the Change in the Resonant Capacitor Voltage, Change in N_f and Change in the $I_{pk,f}$ in Response to Minor Fluctuations in the Peak Pulse Voltage

The resonant capacitor will charge to the required voltage if there is a slight decrement in the peak pulse voltage. However, a slight increment in the peak pulse voltage necessitates greater energy from the resonant capacitor, emphasizing the importance of charging the resonant capacitor within a predefined time, as determined by the charging time (T_{chrg}).

Let the peak pulse voltage increase by Δv_o. Putting $V_{o,\max} = V_{o,\max} + \Delta v_o$ in

$$E'_{C_o} = \frac{1}{2}C_o(V_{o,\max} + \Delta v_o)^2 \tag{31}$$

$$E'_{C_r} = E'_{C_o} - E_{C_{Q1}} + \frac{1}{2}L_r I_{pk,r}^2. \tag{32}$$

The change in the energy of the resonant capacitor is given by

$$\begin{aligned}\Delta E_{C_r} &= E'_{C_r} - E_{C_r} \\ &= C_o V_{o,\max}\Delta v_o.\end{aligned} \tag{33}$$

For a constant $V_{C_{r,\max}}$, let $V_{C_{r,\min}}$ decreases by $\Delta v_{C_{r,\min}}$. Putting $E_{C_r} = E_{C_r} + \Delta v_o V_{o,\max}C_o$ and $V_{C_{r,\min}} = V_{C_{r,\min}} - \Delta v_{C_{r,\min}}$

$$\Delta v_{C_{r,\min}} = \frac{\Delta v_o V_{o,\max}C_o}{C_r V_{C_{r,\min}}}. \tag{34}$$

The minimum voltage attained by the resonant capacitor is given by $(V_{C_{r,\min}} - \Delta v_{C_{r,\min}})$. If $(V_{C_{r,\min}} - \Delta v_{C_{r,\min}}) > 0$, then no change in $I_{pf,f}$ is required to charge the resonant capacitor within $T_{\text{chrg(max)}}$. But if $(V_{C_{r,\min}} - \Delta v_{C_{r,\min}}) < 0$, in this case $V_{C_{r,\max}}$ needs to be increased. Similarly approach is followed for derivation of $\Delta v_{C_{r,\max}}$

$$\Delta v_{C_{r,\max}} = \frac{\Delta v_o V_{o,\max}C_o}{C_r V_{C_{r,\max}}}. \tag{35}$$

Thus, the maximum voltage attained by the resonant capacitor is given by $(V_{C_{r,\max}} + \Delta v_{C_{r,\max}})$. The new optimal peak current is obtained by putting $(V_{C_{r,\max}} + \Delta v_{C_{r,\max}})$ in (22) and (23). The instant $(V_{C_{r,\min}} - \Delta v_{C_{r,\min}}) < 0$ is detected by the controller and it increases the peak current to the new optimal value, as given in

$$I'_{pk,f} = \sqrt{\frac{1}{\eta_f L_{m_f}}\left[2E'_{C_{r,\text{cycle}}} + C_{f,\text{eff}}\left(V_{C_{r,\max}}^2 - n_1^2 V_{\text{dc}}^2\right)\right]} \tag{36}$$

where

$$E'_{C_{r,\text{cycle}}} = \frac{C_r\left(V_{C_{r,\max}}^2 - V_{C_{r,\min}}^2 + \frac{2\Delta v_o V_{o,\max}C_o}{C_r}\right)}{2T_{chrg(\max)}f_{Q_1}}. \tag{37}$$

The features of the energy-based model are summarized as follows:

1) The proposed energy-based model is straightforward and offers insights into energy circulation involving dominant parasitics and energy exchanges.

2) The proposed model optimizes the peak current through a control computational block maintaining the charging time and average power less than 150 W, thereby providing programmability in the peak pulse voltage.
3) The proposed model predicts essential parameters such as N_f, $V_{C_{r,\max}}$, $V_{C_{r,\min}}$, $I_{pk,f}$, average output power, and the efficiency of the converter while considering dominant parasitics.

IV. Proposed Control Scheme

The resonant flyback converter operates using a hybrid control scheme. Gating pulses for Q_1 are derived from PCM and MVP control, while for Q_2, they are derived from the PRR and FWHM of the pulse voltage profile.

A. Conventional Peak Current and MVP Control

The green color box in Fig. 2 shows the conventional peak current and MVP control scheme of the pulse generator. At t_3, Q_1 is turned ON, and current through i_l begins to rise. Once it reaches the set peak current reference ($I_{pk,f}$), PCM control scheme turns OFF Q_1 (refer to Fig. 4). This is accomplished by detecting the switch current via a CT and reducing it to an equivalent voltage for the controller. During the interval t_7 to t_8, as the voltage across Q_1 falls below V_{dc}, its body diode turns ON to transfer the energy stored in L_{m_f} back to the source. At this instant, the gating pulses for turning ON Q_1 are provided to achieve ZVS. This process involves sensing the voltage across Q_1 and input voltage V_{dc} using voltage sensors, and when $v_{Q_1} < V_{\text{dc}}$, Q_1 is turned ON with a slight delay. This turn-ON sequence is known as the MVP control scheme. In this control scheme, the turn-OFF time for Q_1 varies with the resonant capacitor voltage, leading to a variable switching frequency of Q_1 ranging from $f_{Q_{1,\min}}$ to $f_{Q_{1,\max}}$. This is due to the fact that as the resonant capacitor voltage changes, the energy absorbed by the parasitic capacitance also changes, resulting in varying energy being transferred to the resonant capacitor in each switching interval of Q_1 (see Section III-B). Therefore, precise sensing of v_{Q_1} is necessary to ensure precise turn-ON instant. This process repeats in subsequent cycles until v_{C_r} reaches $V_{C_{r,\max}}$, upon which the peak current flowing through the magnetizing inductance of LVT is reduced to $I_{pk,f(\min)}$ to supply for the energy losses in the parasitics (see Section III-B). This is achieved by sensing v_{C_r} through a voltage sensor. So, three voltage sensors and a current sensor are required to implement conventional peak current with MVP control scheme.

B. Proposed Predictive Variable Frequency Control Scheme

The proposed predictive control scheme of the pulse generator, depicted in the blue box of Fig. 1, is utilized to generate the gating signals for both Q_1 and Q_2, as detailed in this section.

1) Sampler Block: The instantaneous output voltage of the resonant capacitor (v_{C_r}) is sampled at every rising edge of the turn-ON instant of Q_1 and is taken to the computational block for every kth sample, where $k = 0, 1, 2 \ldots N_f$. The discretized $v_{C_r}(t)$ is shown in the following:

$$v_{C_r}(k) = \sqrt{\frac{L_{m_f} I_{pk,f}^2 + (n_1 V_{\text{dc}})^2 C_{f,\text{eff}} + C_r v_{C_r}^2(k-1)}{C_r + C_{f,\text{eff}}}}. \tag{38}$$

2) Computational Block: From Fig. 4, let,

$$\begin{aligned} t_1 - t_0 &= t'_{on,Q2} \\ t_4 - t_3 &= t'_{on,Q1} \\ t_5 - t_4 &= t_{r1} \\ t_6 - t_5 &= t_d \\ t_7 - t_6 &= t_{r2} \\ t_8 - t_7 &= t_{bd}. \end{aligned} \tag{39}$$

The sensed resonant capacitor voltage $v_{C_r}(k)$, T_{fwhm} and the F_{pulse} (obtained from the pulse voltage profile) is utilized to compute all the timing intervals of the resonant flyback converter, and arrive at the turn-ON and turn-OFF timing intervals for Q_1 and Q_2 as detailed from

$$t'_{\text{on},Q2} = 2\left(T_{\text{fwhm}} - \frac{\pi}{3w_{r2}}\right) \tag{40}$$

$$t'_{\text{on},Q1} = \frac{(L_{m_f} + L_{lkf})}{V_{\text{dc}}} I_{pk,f} \tag{41}$$

$$t_{r1}(k+1) = \frac{1}{w_{f_1}}\left[\cos^{-1}\left(\frac{-v_{C_r}(k)}{n_1 w_{f_1} L_{m_f} I_m}\right) - \phi_1\right] \tag{42}$$

$$t_d(k+1) = \frac{1}{w_{f_2}}\left(\frac{\pi}{2} - \phi_2\right) \tag{43}$$

$$t_{r2}(k+1) = \frac{1}{w_{f_1}}\left[\pi - \cos^{-1}\left(\frac{n_1 V_{\text{dc}}}{v_{C_r}(k)}\right)\right] \tag{44}$$

$$t_{bd}(k+1) = \frac{v_{C_r}(k)}{n_1 w_{f_1} V_{\text{dc}}} \sin\left[w_{f_1} t_{r2}(k+1)\right] \tag{45}$$

where

$$w_{r_2} = \sqrt{\frac{1}{(L_r + L_{lkr}) C_{r,\text{eff}}}} \tag{46}$$

$$w_{f_1} = \frac{1}{n_1 \sqrt{(L_{m_f} + L_{lkf}) C_{f,\text{eff}}}} \tag{47}$$

$$w_{f_2} = \frac{1}{n_1 \sqrt{(L_{m_f} + L_{lkf})\, C_r}} \tag{48}$$

$$I_m = \sqrt{I_{pk,f}^2 + \left(\frac{V_{\text{dc}}}{w_{f_1}\left(L_{m_f} + L_{lkf}\right)}\right)^2} \tag{49}$$

$$\phi_1 = \tan^{-1}\left(\frac{I_{pk,f} w_{f_1}\left(L_{m_f} + L_{lkf}\right)}{V_{\text{dc}}}\right) \tag{50}$$

$$\phi_2 = \tan^{-1}\left(\frac{v_{C_r}(k)}{n_1 w_{f_2} L_{m_f} I_{pk,f}}\right). \tag{51}$$

The aforementioned time intervals from (41)–(45) are provided to the "MOSFET Q_1 Time Predictor Block" and the time interval in (40) is provided to "MOSFET Q_2 Time Predictor Block" to determine the gating pulses for Q_1 and Q_2, respectively.

3) MOSFET Q_1 and Q_2 Time Instant Predictor and Modulator Block: The MOSFET Q_1 time predictor block predicts the turn-ON and turn-OFF time instant for Q_1 before sending it to the modulator block. The turn-OFF time or the turn-ON instant for $k+1$th sample is defined as follows:

$$t_{\text{off},Q1}(k+1)=t_{r1}(k+1)+t_d(k+1)+t_{r2}(k+1)+\alpha t_{bd}(k+1) \tag{52}$$

where

$$\alpha = \frac{n_1 V_{\text{dc}} \cos^{-1}\left[n_1 V_{\text{dc}}/v_{C_r}(k)\right]}{w_{f_1} v_{C_r}(k) t_{r2}(k+1)}. \tag{53}$$

During the Q_1 body diode conduction interval (t_{bd}), the turn-ON pulse to Q_1 is provided. To achieve ZVS, the turn-OFF duration is modulated by multiplying α with t_{bd}, ensuring that the turn-ON instant occurs within t_{bd}. The remaining time interval of t_{bd} must be considered in calculating the turn-ON time. Therefore, the turn-ON time or turn-OFF instant for the $(k+1)$th sample is specified in

$$t_{on,Q1}(k+1) = t'_{on,Q1} + [1-\alpha]\, t_{bd}(k+1). \tag{54}$$

The switching frequency of Q_1 is calculated and provided in the following:

$$f_{Q1}(k+1) = \frac{1}{t_{\text{on},Q1}(k+1) + t_{\text{off},Q1}(k+1)} \tag{55}$$

where the minimum and maximum switching frequency are determined by substituting $k=0$ and $k=N_f$ into the expression given in (55), respectively.

Similarly, the MOSFET Q_2 time predictor block predicts the turn-ON and turn-OFF time instant for Q_2 before sending it to the modulator block. The turn-OFF instant to Q_2 is delayed by a factor $\beta = 1+(\frac{w_{r1}}{w_{r2}})$, ensuring Q_2 turns OFF during the body diode conduction interval (i.e., t_1 to t_2), ensuring ZCS. Therefore, the turn-ON and turn-OFF time for Q_2 is given in (56) and (57), respectively

$$t_{\text{on},Q2} = \beta t'_{\text{on},Q2} \tag{56}$$

$$t_{\text{off},Q2} = T_{\text{pulse}} - \beta t'_{\text{on},Q2}. \tag{57}$$

The variables $t_{\text{on},Q1}(k+1), t_{\text{off},Q1}(k+1), f_{\text{sw},1}(k+1), t_{\text{on},Q2}$, and $t_{\text{off},Q2}$ are passed to the variable PWM modulator block, which generates gating pulses for Q_1 and Q_2. Once $v_{C_r}(k)$ reaches $V_{C_{r,\text{ref}}}$, the peak current flowing through the magnetizing inductance of LVT is reduced from $I_{pk,f}$ to $I_{pk,f(\text{min})}$ to compensate for energy losses in the parasitics of the converter (refer to Section III-B). Fig. 5 depicts the flowchart for the proposed control scheme.

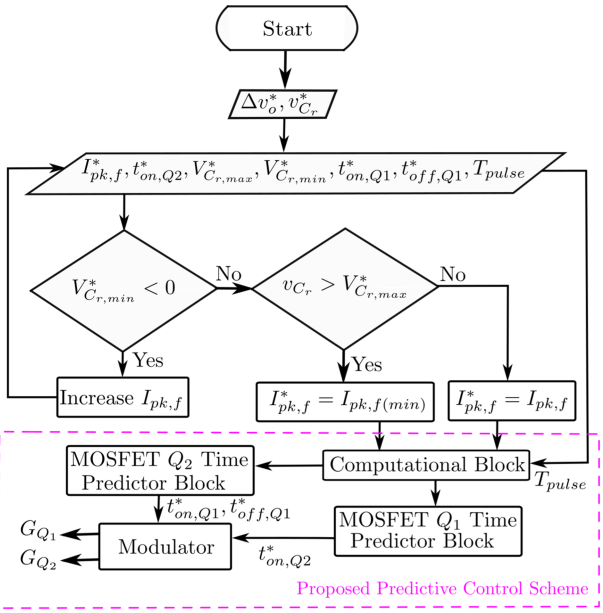

Fig. 5. Flowchart of the proposed control scheme.

C. Proposed Control Scheme Implementation and Timing Analysis

The proposed control scheme is implemented on the Texas Instruments TMS320F28379D processor, featuring a system clock frequency of 200 MHz and 12-bit analog to digital converters (ADCs) operating at a maximum clock frequency of 50 MHz. The voltage across the resonant capacitor is sensed and scaled at every kth sample and fed to the ADC. The acquisition window of the sample and hold is set to 180 ns to accurately capture the kth sample data. After acquisition, the data are converted into its digital equivalent by the 12-bit ADC. Typically, the start of conversion (SOC) to end of conversion (EOC) for the ADC requires 44 system clock cycles, equivalent to 220 ns ($44 * 5$ ns). Hence, the digital equivalent of the resonant capacitor voltage ($v_{C_r}(k)$) becomes available after $t_{(k)adc} = 400$ ns [as illustrated in Fig. 6(a)].

The digital value is given to the computational block and the MOSFET Q_1 time predictor block, which computes the values of $t_{\text{on},Q1}(k+1)$, $t_{\text{off},Q1}(k+1)$ and $f_{Q1}(k+1)$. The reference signal value ($C_{Q1}(k+1)$) and the counter peak value ($T_{Q1}(k+1)$) of Q_1 are computed precisely in the modulator block and the gating pulses for the $k+1$th sample is derived [see shown in Fig. 6(a)]

$$T_{Q1}(k+1) = \frac{f_{\text{epwm,clk}}}{f_{Q1}(k+1)} \tag{58}$$

$$C_{Q1}(k+1) = f_{\text{epwm,clk}} t_{\text{on},Q1}(k+1) \tag{59}$$

where $f_{\text{epwm},clk}$ is the ePWM clock frequency of TMS320F28379D, i.e., 100 MHz. Similarly, the computational block and MOSFET Q_2 time prediction block computes the values of $t_{\text{on},Q2}$ and $t_{\text{off},Q2}$. The reference signal value (C_{Q2}) and the counter peak value (T_{Q2}) of Q_2 are computed precisely in the modulator block, and the gating pulses are derived [as shown in Fig. 6(b)]

$$T_{Q2} = \frac{f_{\text{epwm,clk}}}{f_{\text{pulse}}} \tag{60}$$

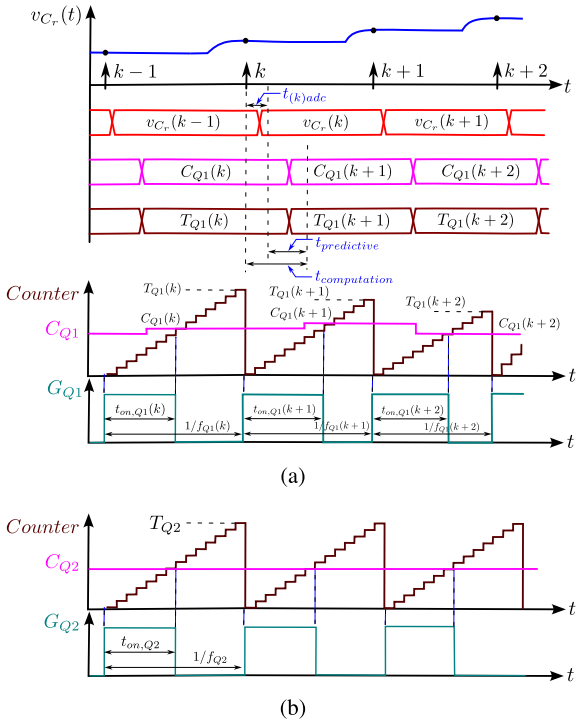

Fig. 6. (a) Timing diagram and Q_1 gating pulse generation. (b) Q_2 gating pulse generation for the proposed predictive variable frequency control scheme.

$$C_{Q2} = f_{\text{epwm,clk}} t_{\text{on},Q2}. \tag{61}$$

In this work, the total delay for predictive computation of counter value and the reference signal value for both Q_1 and Q_2 ($t_{\text{predictive}}$) comes to be 1.44 μs, resulting in a total computational time delay of 1.84 μs, as specified in the following:

$$t_{\text{computation}} = t_{(k)\text{adc}} + t_{\text{predictive}}. \tag{62}$$

D. Control Complexity and Computational Burden

- *Discretization of Time-Domain Parameters:* The complex time-domain equations for determining the turn-ON and turn-OFF timings of Q_1 and Q_2 are discretized into the z-domain using Laplace transforms and Bilinear transformations, facilitating their implementation in the DSP.
- *Capacitor Voltage Sensing:* To sense the resonant capacitor voltage, an op-amp-based sensing circuit (TL064ACDR IC) is implemented in the hardware. The voltage is scaled down from 0–300 V to 0–3.3 V, ensuring compatibility with the input limits of the DSP.
- *ADC Configuration and Implementation:* The scaled resonant capacitor voltage is sampled with a 180 ns acquisition window. After acquisition, the dataare converted into its digital equivalent by the 12-bit ADC with the SoC triggered by an ePWM interrupt at every rising edge of G_{Q_1}.
- *Predictive Algorithm:* The predictive control algorithm is implemented in ePWM ISR, which was configured for the ADC SoC. The algorithm takes the digital value of the sampled resonant capacitor voltage, T_{fwhm} and F_{pulse} to compute the values of $t_{on,Q1}(k+1)$, $t_{off,Q1}(k+1)$, $f_{Q1}(k+1)$, $t_{on,Q2}(k+1)$ and $t_{off,Q2}(k+1)$.

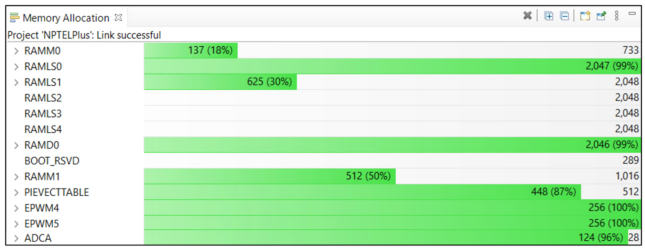

Fig. 7. Memory allocation in the F28379D DSP for the proposed predictive control implementation.

- *Gating pulses generation for Q_1 and Q_2:* In F28379D, the TBCTR (Time Base Counter) resister generates the carrier signal with its peak values stored in TBPRD (Time Base Period) resister and the clock stored in TBCLK (Time base clock) register. The CMPA (Compare A) register holds the reference signal value. In order to generate the gating pulses for Q_1, TBPRD and CMPA for Q_1 are assigned to $T_{Q_1}(k)$ and $C_{Q_1}(k)$, respectively. Similar assignments apply to Q_2.
- *Protection:* The ePWM Trip Zone module monitors the resonant capacitor voltage and disables the ePWM if overvoltage or overcurrent conditions occur, protecting the converter from abnormalities.

Fig. 7 illustrates the computational burden and memory allocation across key memory regions in the F28379D DSP. The predictive control algorithm is executed on RAMLS0 and RAMLS1, while ADCA converts the resonant capacitor voltage into its digital equivalent. EPWM4 triggers the SoC for ADCA and generates gating pulses for Q_1. EPWM5 handles gating pulses for Q_2. The EPWM4 interrupt is enabled in PEVECTTABLE. RAMM0, RAMD0, and RAMM1 manage system initialization, GPIO setup, and ePWM Trip Zone functions. The memory footprint for these operations is approximately 9.15 kB, utilizing 0.915% of the available 1 MB memory in DSP.

V. Design Guidelines

The design guidelines of the HV pulse generator are shown in this section.

A. Resonant Capacitor (C_r), Resonant Inductor (L_r) and Turns Ratio of HVT (n_2)

The turns ratio of the HVT is chosen based on the stress on Q_2 and is specified in (63). The value of C_r is determined from the energy balance equation presented in (4) and is provided in (64). The resonant capacitor charges up to a maximum value of $V_{C_{r,\max}}$ and is given in (65)

$$n_2 = \frac{V_{o,\max}}{V_{C_{r,\max}} - \sigma_{Q_2} V_{bd,Q2}} \tag{63}$$

$$C_r = \frac{C_o}{\chi}\left(\frac{V_{o,\max}}{V_{C_{r,\max}}}\right)^2 - C_{Q2} \tag{64}$$

$$V_{C_{r,\max}} = \frac{V_{o,\max}}{2 n_2 C_r}\left[n_2^2 (C_o + C_{wr}) + C_r\right] \tag{65}$$

where σ_{Q_2} is the margin factor (typically < 1), $V_{bd,Q2}$ is the break down voltage of Q_2 and χ is the energy efficiency factor for resonant capacitor (usually < 1). By solving (63), (64), and (65), the value of n_2 and C_r are determined. The value of the resonant inductance (L_r) is determined by using (1) with $w_{r_1} = \frac{2\pi}{T_{\text{rise}}}$.

B. Magnetizing Inductance (L_{m_f}) and Turns Ratio (n_1) of LVT

The magnetizing inductance of LVT (L_{m_f}) is selected based on the minimum and maximum switching frequency of Q_1 as obtained from (55), and the energy released by L_{m_f} during charging of the resonant capacitor from $V_{C_{r,\min}}$ to $V_{C_{r,\max}}$ as detailed in (7) and (8). The turns ratio n_1 is chosen based on the voltage stress experienced by Q_1 and D_{hv}, and is determined from the maximum and minimum turns ratios specified in (66) and (67), respectively

$$n_{1_{\max}} = \frac{(\sigma_D . V_{bd,D}) - V_{C_{r,\max}}}{V_{\text{dc}}} \tag{66}$$

$$n_{1_{\min}} = \frac{V_{C_{r,\max}}}{(\sigma_{Q1} . V_{bd,Q1}) - V_{\text{dc}} - V_{lkp}} \tag{67}$$

where V_{lkp} is the voltage spike caused due to L_{lkf} and $C_{f,\text{eff}}$, σ_{Q1} and σ_D are the margin factor (< 1), and $V_{bd,D}$ and $V_{bd,Q1}$ is the breakdown voltage of D_{hv} and Q_1, respectively.

C. Parasitics of the Pulse Generator

In Fig. 2, the key parasitics are highlighted in red. These dominant parasitics include the switch node parasitics, as well as the leakage inductance and winding capacitance of the transformers. The values for these parasitics are detailed in this section.

1) Leakage Inductance of LVT and HVT: To determine the true leakage inductance, a soldered short circuit is applied to the secondaries of both the HVT and the LVT. The LCR meter is then connected to the primary windings of the transformers. The inductance value measured by the LCR meter is recorded as the true leakage inductance. The measured values for L_{lkf} and L_{lkr} are 183 nH and 30 μH, respectively.

2) Winding Capacitance of LVT and Switch Node Capacitance of Q_1 and D_{hv}: To determine the winding capacitance of LVT, a single gating pulse is applied to Q_1 while no pulse was applied to Q_2. As shown in Fig. 8, once v_{C_r} increases and settles, the voltage across Q_1 oscillates with frequency $f_{\text{osc},f} = \frac{1}{\Delta t_{\text{osc},f}}$ = 666.67 kHz. This oscillation occurs because the residual energy in $C_{f,\text{eff}}$ oscillates with L_{mf}. Hence, the value of $C_{f,\text{eff}}$ is obtained in the following:

$$C_{f,\text{eff}} = \frac{1}{(2\pi n_1 f_{\text{osc},f})^2 L_{m_f}}. \tag{68}$$

IMW120R220M1H type SiC MOSFET and GP3D005A170B type SiC diode is used for Q_1 and D_{hv}, respectively. The value of switch node capacitance of Q_1 and D_{hv} is determined from the data sheet of the components. Thus, the value of the winding capacitance of LVT is obtained in

$$C_{wf} = C_{f,\text{eff}} - \frac{C_{Q1}}{n_1^2} - C_{\text{hvd}}. \tag{69}$$

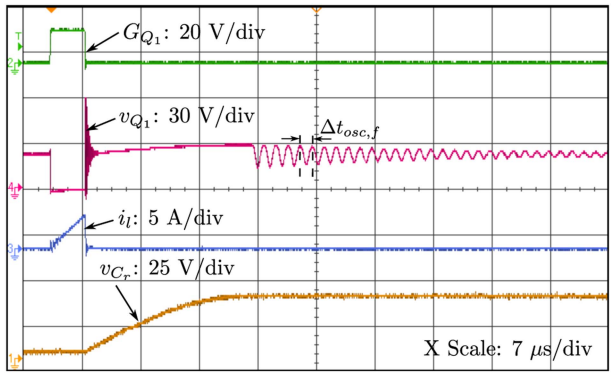

Fig. 8. Experimental results determining the equivalent flyback parasitic capacitance ($C_{f,\text{eff}}$).

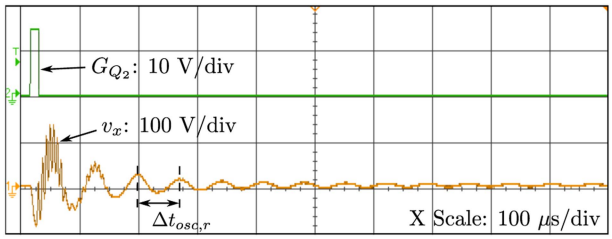

Fig. 9. Experimental results determining the equivalent resonant parasitic capacitance ($C_{r,\text{eff}}$).

3) Winding Capacitance of HVT and Switch Node Capacitance of Q_2: To determine the winding capacitance of HVT, a single gating pulse was applied to Q_2 while no pulse was applied to Q_1. As shown in Fig. 9, the voltage across the secondary terminals of the HVT (v_x) oscillates with frequency $f_{\text{osc},r} = \frac{1}{\Delta t_{\text{osc},r}} =$ 13.34 kHz. Hence, the value of $C_{r,\text{eff}}$ is obtained in the following:

$$C_{r,\text{eff}} = \frac{1}{(2\pi f_{\text{osc},r})^2 L_{m_r}}. \tag{70}$$

IMW120R220M1H type SiC MOSFET is used for Q_2 and the value of switch node capacitance of Q_2 is determined from the data sheet of the component. Thus, the value of the winding capacitance of HVT is obtained in the following:

$$C_{wr} = \frac{C_D C_o}{C_o + C_D} + \frac{C_{Q2} C_{r,\text{eff}}}{n_2^2 (C_{Q2} - C_{r,\text{eff}})}. \tag{71}$$

D. Effect of Nonlinearity in the MOSFET and Diode Parasitics

During steady-state operation, to obtain a pulse output of -2.5 kV, the voltage across the resonant capacitor ranges from 150 to 105 V. As a result, the drain-to-source voltage across MOSFET Q_1 (v_{Q_1}) varies from 62.88 to 52.41 V. The high-voltage diode (D_{hv}) experiences voltages ranging from 270.4 to 225.4 V, and D_b consistently has 2.5 kV. The maximum drain-to-source voltage across MOSFET Q_2 (v_{Q_2}) is 150 V.

The MOSFETs Q_1 and Q_2 are SiC devices (Part number IMW120R220M1H), and the diodes D_{hv} and D_b are SiC Schottky diodes (Part number GP3D010A170B), with D_b configured with three diodes in series to achieve the necessary breakdown

TABLE I
POWER SUPPLY REQUIREMENTS FOR PPT

Peak pulse voltage ($V_{o,max}$)	250 V to 2.5 kV
Pulse width or FWHM (T_{fwhm})	20 μs
Rise time (T_{rise})	10 μs
Pulse repetitive rate (F_{pulse})	1000 Hz
Average pulse power (P_{C_o})	140 W @2.5 kV
Input voltage (V_{dc})	28 V

TABLE II
DESIGNED AND CONTROL PARAMETERS OF THE HV PULSE GENERATOR

Resonant inductance (L_r)	35 μH
Resonant capacitance (C_r)	0.3 μF
Turns ratio of HVT (n_2)	10
Magnetising inductance of LVT (L_{m_f})	25 μH
Turns ratio of LVT (n_1)	5
Winding capacitance of HVT (C_{wr})	282.8 pF
Winding capacitance of LVT (C_{wf})	70.7 pF
Optimal peak current of Q_1 ($I_{pk,f}$)	3.5 A
Switching frequency of Q_1	33–142 kHz
Turn-on time of Q_2	15 μs
Switching frequency of Q_2	1 kHz

voltage. From the datasheets of the MOSFET and diode, the parasitic capacitance of the MOSFET Q_1 remains nearly constant between 62.88 and 52.41 V and similarly, the diodes' capacitance is steady between 270.4 and 225.4 V at a fixed operating point. The values of the parasitic capacitances in Q_2 and D_b do not vary. However, capacitance does vary with different operating points, and this variation is integrated into the control model using a curve-fitting technique based on the parasitic characteristics of the MOSFETs and diodes. This approach improves control accuracy and enhances the predictive performance of the system.

E. Parametric Values of the Pulse Generator

The specifications for the power supply of the PPT are provided in Table I. The parameters for the HV pulse generator, as derived from the design guidelines and the energy-based model (refer Section III), are listed in Table II.

VI. EXPERIMENTAL VERIFICATION

The HV pulse generator prototype for the PPT is built and depicted in Fig. 10. The proposed energy-based model and predictive control scheme are experimentally validated based on the specifications provided in Tables I and II.

Fig. 11 illustrates the pulsed output of −2.5 kV with a PRR of 1000 Hz, achieved with the proposed control scheme enabled. The MOSFET Q_2 time predictor block accurately calculates the turn-ON time for Q_2, as indicated by G_{Q_2} using the FWHM (T_{fwhm}) and PRR (F_{pulse}). During the gating pulse to Q_2, the voltage across the resonant capacitor (v_{C_r}) decreases from 150 to 102.5 V and subsequently charges back to 150 V before the next gating pulse to Q_2. The charging time (T_{chrg}) is 562.5 μs, significantly shorter than the maximum allowable charging time ($T_{\text{chrg(max)}}$) of 980 μs. A consistent peak current of 3.5 A is maintained to achieve the charging of C_r. The average output pulse power is calculated as 139.68 W, aligning with the specifications listed in Table I.

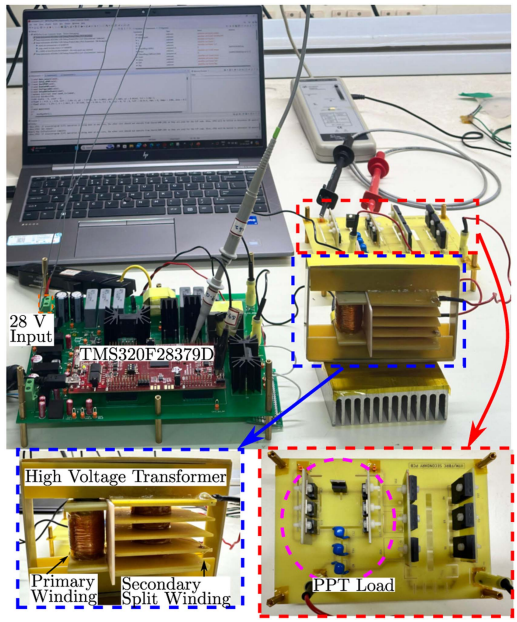

Fig. 10. Experimental setup for HV pulse generator with proposed predictive control technique.

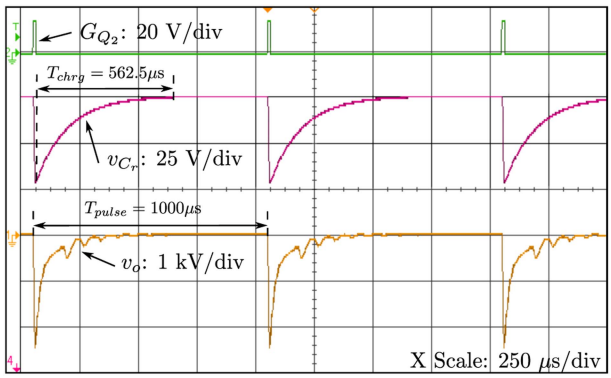

Fig. 11. Experimental steady-state waveforms of the HV pulse generator at a −2.5 kV pulsed output, showing G_{Q_2}, v_{C_r} and v_o.

Fig. 12 shows a single switching cycle of Q_2, highlighting a pulse rise time (T_{rise}) of 10μs and a FWHM of 20μs, which aligns with the specifications in Table I. The output voltage (v_o) decreases from $0.16 * V_{o,\text{max}}$ to zero, oscillating at a frequency $f_{\text{osc},r}$, as detailed in Section V-C3, due to the energy exchanges between the parasitic capacitances and the magnetizing inductance of the HVT.

Fig. 13 shows the resonant inductor current achieves a peak current ($I_{pk,r}$) of 2.7 A. Q_2 is turned OFF during the negative i_{L_r} current, indicating ZCS turn OFF of Q_2. Fig. 14 illustrates the charging of v_{C_r} from $V_{C_{r,\text{min}}}$ to $V_{C_{r,\text{max}}}$ with the proposed control scheme enabled. The MOSFET Q_1 time predictor block accurately calculates the turn-ON and turn-OFF times for Q_1, as indicated by G_{Q_1}, using the sampled resonant capacitor voltage. v_{C_r} is sampled at the kth instant, and the turn-ON and turn-OFF

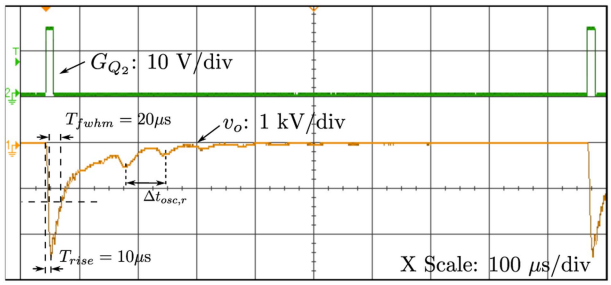

Fig. 12. Experimental steady-state waveforms of the HV pulse generator at a -2.5 kV pulsed output, showing G_{Q_2} and v_o for a single switching cycle of Q_2.

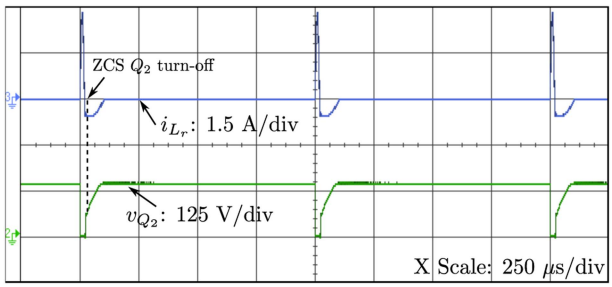

Fig. 13. Experimental steady-state waveforms of the HV pulse generator at a -2.5 kV pulsed output, showing i_{L_r} and v_{Q_2}.

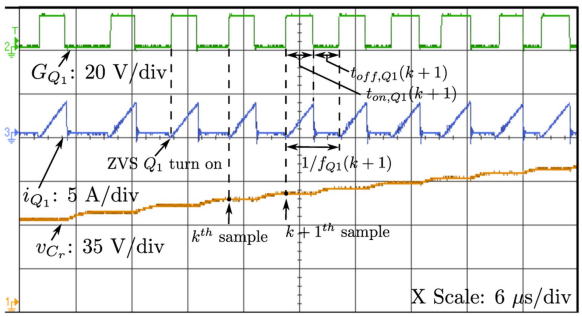

Fig. 14. Experimental waveforms of the charging of voltage across the resonant capacitor (v_{C_r}) from $V_{C_{r,\min}}$ to $V_{C_{r,\max}}$, indicating G_{Q_1} and i_{Q_1}.

times for the $(K+1)$th instance are predicted by the MOSFET Q_1 time predictor block. The predictive control achieves PCM control for turning OFF Q_1 and MVP control for turning on Q_1 with ZVS. The number of cycles (N_f) required to charge the resonant capacitor is 37, which is consistent with the equation given in (25).

Fig. 15(a) shows a comparison between the actual and predicted turn-ON times of Q_1, with observed errors ranging from 0.1% to 1%. Similarly, Fig. 15(b) compares the actual and predicted turn-OFF times of Q_1, with errors ranging from 3% to 4%. In addition, Fig. 15(c) presents a comparison between the actual and predicted frequencies of Q_1, with errors ranging from 2.5% to 3%. This error in the turn-ON, turn-OFF time and frequency calculation is minimal and attributed to the discretization of sensed parameters and the resolution or step size of the digital

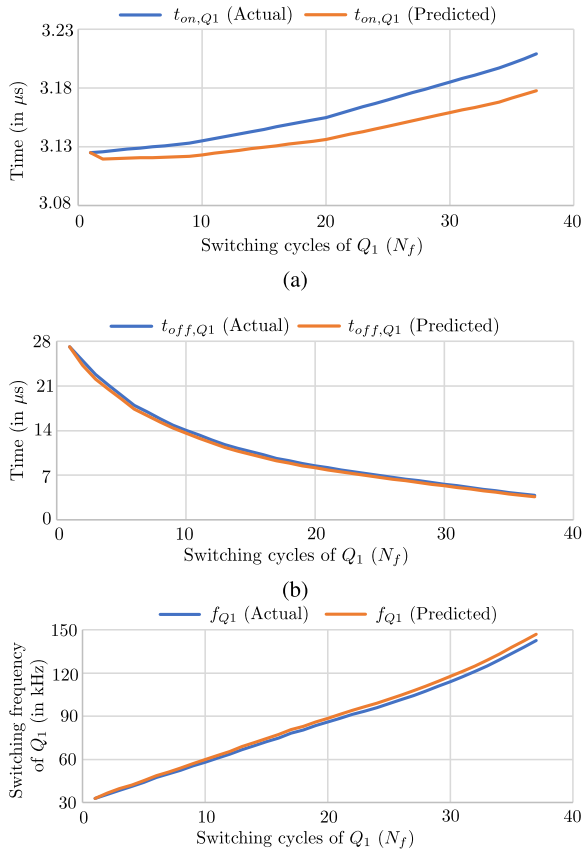

Fig. 15. (a) Turn-ON time of Q_1, (b) turn-off time of Q_1, (c) frequency of Q_1 with respect to switching cycles of Q_1.

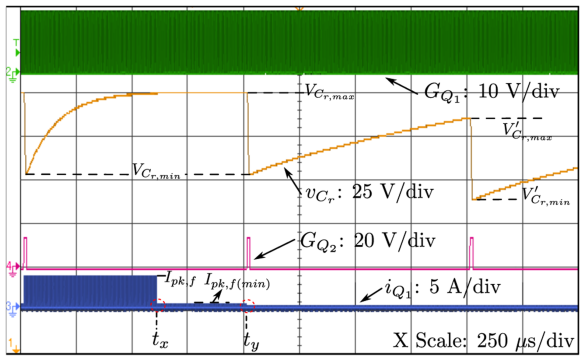

Fig. 16. Experimental waveforms of charging of the resonant capacitor for $I_{pk,f} > I_{pk,f(\min)}$ and $I_{pk,f} < I_{pk,f(\min)}$.

up counter. The error in the predicted values does not impact N_f, so the charging process remains largely unaffected.

As shown in Fig. 16, until t_x, $I_{pk,f}$ is maintained at 3.5 A, and v_{C_r} is charged to $V_{C_{r,\max}}$ within 562.5 μs. Once v_{C_r} reaches $V_{C_{r,\max}}$, $I_{pk,f}$ is reduced to $I_{pk,f(\min)} = 0.8$A to supply for the circulating energy of $C_{f,\text{eff}}$. At t_y, $I_{pk,f}$ is further reduced to less than $I_{pk,f(\min)}$, specifically to 0.5 A, causing v_{C_r} to fall short of reaching the desired $V_{C_{r,\max}}$ before the next gating pulse of Q_2. This leads to a decrease in the output peak pulse amplitude.

To achieve programmability in the pulsed output voltage, the voltage across the resonant capacitor is varied by varying

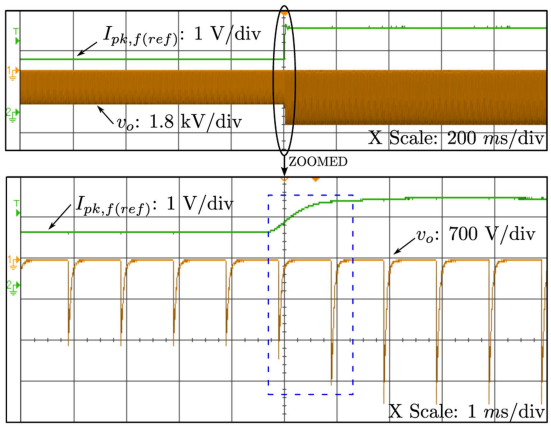

Fig. 17. Experimental waveforms for programmability in the peak voltage of the pulse generator.

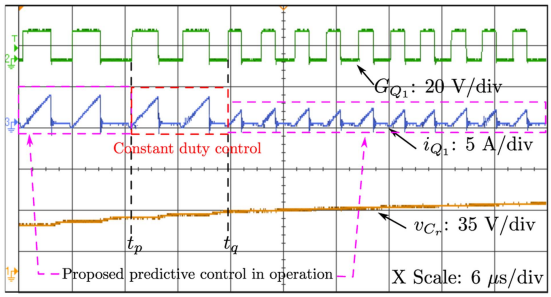

Fig. 18. Experimental waveforms of predictive control scheme operation in transient condition.

the peak current of Q_1. Fig. 17 illustrates the experimental waveform of programmability in the pulse generator's peak output voltage. The peak current reference in DSP is converted to a scaled analog voltage (0 to 3 V) by the built-in DAC, and is displayed in green as $I_{pk,f(ref)}$. Initially $I_{pk,f(ref)}$ is set to 2 A (i.e., analog equivalent of 1.2 V), producing a peak output voltage of -1.5 kV. A linear ramp variation in $I_{pk,f(ref)}$ from 2 to 3.5 A over 1.5 ms raises the peak output voltage to -2.5 kV. The zoomed view highlights that two switching cycles of Q_2 are required to stabilize at the desired voltage, marked in blue in Fig. 17.

Fig. 18 illustrates the experimental results obtained by introducing a step change in the peak current, which is done to assess the system's dynamic response and the performance of the proposed predictive control scheme. Until t_p, the predictive control scheme accurately predicts the turn-ON and turn-OFF times for Q_1. At t_p, $I_{pk,f}$ is changed from 3.5 to 2 A. During this period, the predictive control is temporarily suspended for a minimum of two cycles, and the converter operates in a constant duty control mode. Predictive control is re-enabled at t_q, with the updated $I_{pk,f}$, ensuring a seamless transition back to the control scheme.

Effect of Magnetizing Inductance (L_{m_f}) Tolerance: The effect of magnetizing inductance tolerance is examined at a pulse voltage of -2.5 kV, with variations ranging from the nominal inductance value to an additional 20% of the nominal value, while maintaining C_r constant. To verify experimentally, a 5μH inductor is connected in series with L_{m_f}, and its value is adjusted

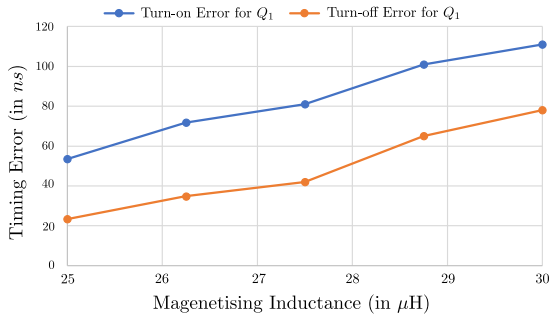

Fig. 19. Turn-ON and turn-OFF timing error for Q_1 for variation in L_{m_f}.

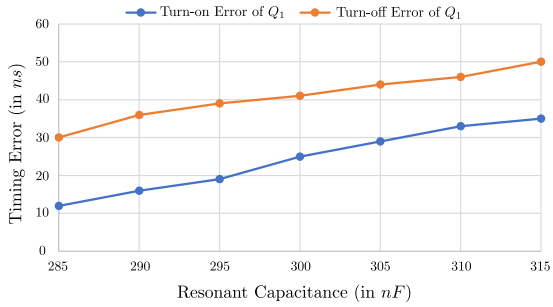

Fig. 20. Turn-ON and Turn-OFF timing error for Q_1 for variation in C_r.

by changing the number of turns. The turn-ON and turn-OFF timing errors of Q_1 are plotted as a function of the inductance variation in Fig. 19. Due to the variation, a maximum turn-ON error of 110 ns results in a minimal peak current deviation of 5.71% at an operating point of -2.5 kV. Despite a maximum turn-OFF error of 80 ns, ZVS turn-ON for Q_1 is consistently maintained in converter operation. Hence, the impact of turn-ON and turn-OFF timing errors in Q_1 on overall efficiency is minimal.

Effect of Resonant Capacitance (C_r) Tolerance:

The most significant factors influencing capacitance variations in resonant circuits are temperature, high voltages, high frequencies, and high rates of voltage change [34]. In the proposed converter, the resonant capacitor operates at a temperature of 30 °C, with a maximum voltage of 150 V at 142 kHz, and a rate of change in voltage of 0.085 V μs^{-1}. Under these conditions, capacitance variations and inaccuracies are minimal. A small variation in the resonant capacitance, ranging from nominal values to $\pm$ 5%, is introduced while keeping all other parameters constant. The resulting turn-ON and turn-OFF timing errors are shown in Fig. 20. The errors are in the range of 10 to 50 ns, which are negligible compared to the turn-ON and turn-OFF times of Q_1.

The effect of L_r and C_r variations can be minimized by tracking w_{f_2} using the capture module of the TMS320F28379D [32].

Effect of variation of Load Parameters (R_o and C_o):

In plasma ionization circuits, the values of R_o and C_o fluctuate under high-voltage pulse conditions due to plasma effects altering both parameters. It is essential to evaluate the impact of load parameter tolerance at a pulse voltage of -2.5 kV. The variation of C_o is considered from the nominal value up to an additional 15%, and the variation of R_o from the nominal value up to an additional 40% [33]. The variations in R_o affect the fall time of the pulse but do not influence prediction accuracy. In contrast, variations in C_o do impact the prediction accuracy of

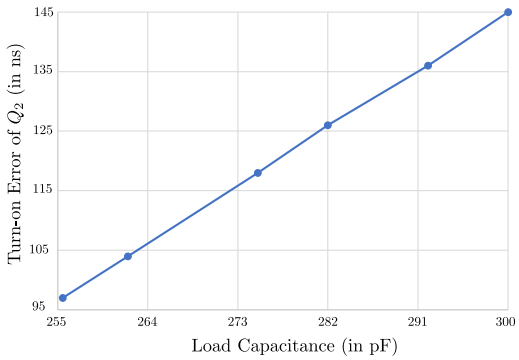

Fig. 21. Turn-ON timing error for Q_2 for variation in C_o.

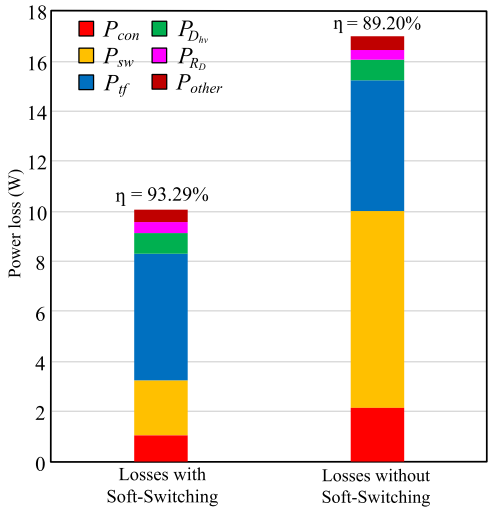

Fig. 22. Detailed power loss breakdown for the pulse generator with a peak pulse voltage of −2.5 kV.

Q_2 [refer to (56) and (57)]. Therefore, the turn-ON timing errors of Q_2 are plotted as a function of variations in C_o in Fig. 21.

As C_o varies, the turn-ON timing error of Q_2 also changes and remains minimal, within the nanosecond range, demonstrating the accuracy of the predictive control. Even with a maximum turn-ON error of 145 ns, the algorithm consistently ensures zero-voltage switching (ZCS) turn-OFF for Q_2 throughout the operation of the converter. The effect of C_o variations can be minimized by tracking w_{r_1} using the capture module of the TMS320F28379D [32].

Loss Analysis for the pulse generator:

The average power loss analysis is performed based on the PPT specifications in Table I and the parameters listed in Table II. RMS and average current values are derived from the voltage and current waveforms, while core losses of the HVT and LVT are referenced from the manufacturer's datasheet. These data points enable the computation of the loss components for the proposed converter. Fig. 22 compares the power loss breakdown of the proposed converter with and without soft switching. The conduction and switching losses of Q_1 and Q_2 are denoted as P_{con} and P_{sw}, respectively. Transformer losses in the HVT and LVT, including contributions from leakage inductance, winding resistance, and core loss, are represented as P_{tf}. The conduction losses in the diode D_{hv} and R_D are denoted as $P_{D_{hv}}$ and P_{R_D}, respectively. Additional losses, such as control circuit losses and conduction losses in L_r, are grouped under P_{other}. A 4% improvement in efficiency is achieved with soft switching, which reduces switching losses compared to hard switching, resulting in lower heat dissipation and enhanced overall converter performance.

Pulse Load Efficiency: Conventional peak current and MVP control systems use three voltage sensors and one CT. For low-power converters, even a slight loss in power can significantly degrade efficiency. Given a peak pulse voltage of −2.5 kV at a power of 140 W, the MOSFET Q_2 must handle approximately 4 A of peak current. With the P8202NLT CT, which has a dc resistance of 0.55 Ω, the conduction loss per CT is about 2.2 W, resulting in a 1.57% reduction in efficiency. The proposed scheme eliminates the need for additional CTs and high-bandwidth current sensors, thereby enhancing power conversion efficiency by avoiding conduction losses. Consequently, the pulse load efficiency, calculated using (30), is observed to be 93.29%.

VII. Conclusion

This article proposes a resonant flyback topology for a high-voltage pulse generator tailored for PPT applications. An energy-based model is utilized to evaluate the impact of parasitics and arrive at the essential design and control parameters of the converter. To ensure a consistent pulse voltage profile, $I_{pk,f}$ is always maintained greater than $I_{pk,f(\text{min})}$. Based on insights from the pulse load profile, a predictive control scheme is introduced for the variable frequency HV pulse generator for precise turn-on and turn-off instants of Q_1 and Q_2. The energy-based model and predictive control scheme are experimentally validated for a pulse load of −2.5 kV with a PRR of 1000 Hz and pulse width of 20 μs, fed from an input voltage of 28 V dc.

The proposed control scheme achieves precise tracking of the MOSFET turn-ON and turn-OFF instants, reducing timing errors to less than 5% compared to conventional control methods. Although conventional control techniques achieve lower timing error than the proposed predictive control, the proposed approach eliminates the need for CT or LEM-based current sensors; thereby improving the efficiency, reducing the cost, and simplifying the converter design. In addition, the low computation time for control implementation ($\leq 2\mu$s or less) enables the converter to operate at high frequencies, thereby enhancing the overall power density of the system. The computation time can be further reduced by leveraging the trigonometric math unit (TMU) and control law accelerator (CLA) available in TMS320F28379D.

References

[1] M. Yaqoob, A. Lashab, J. C. Vasquez, J. M. Guerrero, M. E. Orchard, and A. D. Bintoudi, "A comprehensive review on small satellite microgrids," *IEEE Trans. Power Electron.*, vol. 37, no. 10, pp. 12741–12762, Oct. 2022, doi: 10.1109/TPEL.2022.3175093.

[2] M. LaPointe, E. Strzempkowski, and E. Pencil, "High power MPD thruster performance measurements," in *Proc. 40th AIAA/ASME/SAE/ASEE Joint Propulsion Conf. Exhibit*, 2004, Art. no. 3467, doi: 10.2514/6.2004-3467.

[3] R. Myers, S. Oleson, M. McGuire, N. Meckel, and R. Cassady, *Pulsed Plasma Thruster Technology for Small Satellite Missions*. Washington, DC, USA: NASA 1995.

[4] Z. You, "Chapter 8 - Micropropulsion," in *Space Microsystems and Micro/nano Satellites*. Oxford, U.K.: Butterworth-Heinemann, 2018, pp. 295–339, doi: 10.1016/B978-0-12-812672-1.00008-4.
[5] O. Gorshkov, V. Shutov, K. Kozubsky, V. Ostrovsky, and V. Obukhov, *Development of High Power Magnetoplasmadynamic Thrusters in the USSR*. Moscow, Russia: USSR, 2007.
[6] I. Muzyukin and P. Mikhailov, "Small pulsed plasma thruster based on flashover discharge," in *Proc. IEEE 7th Int. Congr. Energy Fluxes Radiat. Effects*, Tomsk, Russia, 2020, pp. 123–127, doi: 10.1109/EFRE47760.2020.9242173.
[7] M. Kühn and J. Schein, "Pulsed power supply design for vacuum arc thrusters application," in *Proc. IEEE Pulsed Power Plasma Sci.*, Orlando, FL, USA, 2019, pp. 1–4, doi: 10.1109/PPPS34859.2019.9009945.
[8] C. Promislow and J. Little, "Operation and performance of a power processing unit for inductive pulsed plasma thrusters operating at high repetition rates," *IEEE Trans. Plasma Sci.*, vol. 50, no. 9, pp. 3065–3076, Sep. 2022, doi: 10.1109/TPS.2022.3189678.
[9] C. Kuldip and N. Lakshminarasamma, "An energy-based analysis of high voltage resonant-based pulsed low power converter for water treatment application," *IEEE Access*, vol. 12, pp. 49429–49448, 2024, doi: 10.1109/ACCESS.2024.3384574.
[10] Behlke, *High Voltage Push Pull Switching Units*. Taunus, Germany: Behlke, Feb. 2019.
[11] K. Endo et al., "Resonant pulse power supply for compact proton and/or heavy ion synchrotron," 2001. [Online]. Available: https://cds.cern.ch/record/914982
[12] K. Koseki and Y. Shimosaki, "Parasitic resonance in a solid-state pulsed power modulator," *Nucl. Instrum. Methods Phys. Res. Sect. A, Accelerators, Spectrometers, Detectors Assoc. Equip.*, vol. 556, no. 1, 24–30, 2006, doi: 10.1016/j.nima.2005.10.009.
[13] M. Rodriguez et al., "Resonant pulse-shaping power supply for radar transmitters," in *Proc. IEEE 15th Int. Power Electron. Motion Control Conf.*, Novi Sad, Serbia, 2012, pp. LS5e.3-1-LS5e.3-7, doi: 10.1109/EPEPEMC.2012.6397484.
[14] H.-J. Kim, G.-B. Chung, and C. Jae-Ho, "Resonant pulse power converter with a self-switching technique," *J. Power Electron.*, vol. 10, 2010, Art. no. 023652, doi: 10.10.6113/JPE.2010.10.6.784.
[15] R. Erickson and D. Maksimovic, *Fundamentals of Power Electronics*. Heidelberg, Germany: Springer International Publishing, 2020.
[16] P. Thummala, H. Schneider, Z. Zhang, and M. A. E. Andersen, "Investigation of transformer winding architectures for high-voltage (2.5kV) capacitor charging and discharging applications," *IEEE Trans. Power Electron.*, vol. 31, no. 8, pp. 5786–5796, Aug. 2016, doi: 10.1109/TPEL.2015.2491638.
[17] A. V. Bogatyi, V. I. Bogatyi, and S. V. Gordeev, "Development of power processing unit for a low-power ablative pulsed plasma thruster," *IOP Conf. Series, Mater. Sci. Eng.*, vol. 927, no. 1, 2020, Art. no. 012003, doi: 10.1088/1757-899X/927/1/012003.
[18] J. Mcardle, T. G. Wilson, and R. C. S. Wong, "Effects of power-train parasitic capacitance on the dynamic performance of DC-to-DC converters operating in the discontinuous MMF mode," *IEEE Trans. Power Electron.*, vol. PE-2, no. 1, pp. 2–19, Jan. 1987, doi: 10.1109/TPEL.1987.4766327.
[19] S.-S. Hong, S.-K. Ji, Y.-J. Jung, and C.-W. Roh, "Analysis and design of a high voltage flyback converter with resonant elements," *J. Power Electron.*, vol. 10, no. 2, pp. 107–114, Mar. 2010.
[20] S. Gunewardena, W. E. Archer, and R.O. Sanchez, "High voltage miniature transformer design," in *Proc. Elect. Insul. Conf. Elect. Manuf. Coil Winding Conf.*, 2001, pp. 141–147, doi: 10.1109/EEIC.2001.965602.
[21] V. Ravi, S. Satpathy, and N. Lakshminarasamma, "An energy-based analysis for high voltage low power flyback converter feeding capacitive load," *IEEE Trans. Power Electron.*, vol. 35, no. 1, pp. 546–564, Jan. 2020, doi: 10.1109/TPEL.2019.2915565.
[22] S. Sanati and Y. Alinejad-Beromi, "Avoid current transformer saturation using adjustable switched resistor demagnetization method," *IEEE Trans. Power Del.*, vol. 36, no. 1, pp. 92–101, Feb. 2021, doi: 10.1109/TPWRD.2020.2983484.
[23] C. Mitchell, J. A. Dierker, and G. Keyarts, "Current sensing," in *Proc. Int. Telephone Energy Conf.*, Washington, DC, USA, 1978, pp. 322–327, doi: 10.1109/INTLEC.1978.4793569.
[24] L. Chen, S. Shao, Q. Xiao, L. Tarisciotti, P. W. Wheeler, and T. Dragičević, "Model predictive control for dual-active-bridge converters supplying pulsed power loads in naval DC micro-grids," *IEEE Trans. Power Electron.*, vol. 35, no. 2, pp. 1957–1966, Feb. 2020, doi: 10.1109/TPEL.2019.2917450.
[25] D. Zhang, C. Chen, Y. Ou, T. Zheng, and W. Tang, "Model predictive control of three-level bidirectional DC-DC converter based on super capacitor energy storage system," in *Proc. Int. Conf. Elect. Eng.*, Istanbul, Turkey, 2020, pp. 1–5, doi: 10.1109/ICEE49691.2020.9249868.
[26] B. Agrawal, L. Zhou, A. Emadi, and M. Preindl, "Variable-frequency critical soft-switching of wide-bandgap devices for efficient high-frequency nonisolated DC-DC converters," *IEEE Trans. Veh. Technol.*, vol. 69, no. 6, pp. 6094–6106, Jun. 2020, doi: 10.1109/TVT.2020.2987028.
[27] E. F. Reyes-Moraga, "Predictive control of a direct series resonant converter with active output voltage compensation," Ph.D. dissertation, The University of Nottingham, Nottingham, U.K., Feb. 2015.
[28] J. C. A. Prodic, R.W. Erickson, and D. Maksimovic, "Predictive digital current programmed control," *IEEE Trans. Power Electron.*, vol. 18, no. 1, pp. 411–419, Jan. 2003, doi: 10.1109/TPEL.2002.807140.
[29] N. Chitpadi and N. Lakshminarasamma, "Predictive synchronous rectification control scheme for resonant DC–DC converters for battery charging and telecom application," *IEEE J. Emerg. Sel. Topics Ind. Electron.*, vol. 5, no. 4, pp. 1698–1708, Oct. 2024, doi: 10.1109/JESTIE.2024.3393616.
[30] C. Kuldip and N. Lakshminarasamma, "Flyback based resonant converter for high voltage pulsed load application," in *Proc. IEEE Int. Conf. Power Electron. Drives Energy Syst*, Jaipur, India, 2022, pp. 1–7, doi: 10.1109/PEDES56012.2022.10080245.
[31] W. H. Hayt, *Engineering Electromagnetic*, 5th Ed. New York, NY, USA: McGraw-Hill, 1989.
[32] TMS320F2837xD technical reference manual, 2024. [Online]. Available: https://www.ti.com/lit/ug/spruhm8h/spruhm8h.pdf
[33] R. A. Chinga, J. Lin, and S. Roy, "Self-tuning high-voltage high-frequency switching power amplifier for atmospheric-based plasma sterilization," *IEEE Trans. Plasma Sci.*, vol. 42, no. 7, pp. 1861–1869, Jul. 2014, doi: 10.1109/TPS.2014.2328900.
[34] J. Bultitude et al., "Development and characterization of resonant capacitors and inductors for switched tank converters," in *Proc. IEEE Int. Power Electron. Appl. Conf. Expo.*, Shenzhen, China, 2018, pp. 1–6, doi: 10.1109/PEAC.2018.8590395.

Chinara Kuldip (Graduate Student Member, IEEE) received the B.Tech. degree in electrical engineering from the Government College of Engineering, Bhawanipatna, Odisha, India, in 2017, and is currently working toward the dual M.S. and Ph.D. degrees in electrical engineering with the Indian Institute of Technology Madras, Chennai, India.

His research focuses on switched-mode power conversion, high-voltage pulse power applications for water and PFAS treatment, space pulse plasma thrusters, and hydrocarbon synthesis from carbon dioxide. He was among the top recipients to receive the grant in Carbon Zero Challenge 4.0 for his research alignment with sustainable carbon solutions.

Lakshmi Narasamma N (Senior Member, IEEE) received the Ph.D. degree in electrical engineering from the Indian Institute of Science, Bengaluru, India, in 2009.

She is currently a Professor with the Department of Electrical Engineering, Indian Institute of Technology Madras, Chennai, India. Prior to this, she had put in four years in academics. She was a Software Engineer with I2 Technologies India Private Limited and a Systems Specialist with GE Healthcare India Limited. She has authored or coauthored several journal papers in peer-reviewed journals, including IEEE TRANSACTIONS ON POWER ELECTRONICS and several premier conferences, and holds eight patents on power conversion systems related to space and defence applications. Her research interests include power electronics, switched-mode power conversion, and renewable energy systems.

Dr. Lakshmi narasamma was the recipient of the SERB Power Fellowship Outstanding Women Researcher Award 2022 from the Department of Science and Technology and the prestigious Bimal KBose Award 2022 from the Institute of Electronics and Telecommunications for outstanding contributions in the area of power electronics. She is a Fellow of the Institute of Engineers (India).